Observation of Anderson phase in a topological photonic circuit

Jun Gao,[1,*] Ze-Sheng Xu,[1] Daria A. Smirnova,[2] Daniel Leykam,[3] Samuel Gyger,[1] Wen-Hao Zhou,[4,5] Stephan Steinhauer,[1] Val Zwiller,[1] and Ali W. Elshaari[1,†]

[1]*Department of Applied Physics, Royal Institute of Technology, Albanova University Centre, Roslagstullsbacken 21, 106 91 Stockholm, Sweden*
[2]*Nonlinear Physics Centre, Research School of Physics, Australian National University, Canberra ACT 2601, Australia*
[3]*Centre for Quantum Technologies, National University of Singapore, 3 Science Drive 2, Singapore 11754*
[4]*Center for Integrated Quantum Information Technologies (IQIT), School of Physics and Astronomy and State Key Laboratory of Advanced Optical Communication Systems and Networks, Shanghai Jiao Tong University, Shanghai 200240, China*
[5]*CAS Center for Excellence and Synergetic Innovation Center in Quantum Information and Quantum Physics, University of Science and Technology of China, Hefei, Anhui 230026, China*

(Received 21 January 2022; accepted 24 August 2022; published 19 September 2022)

Disordered systems play a central role in condensed matter physics, quantum transport, and topological photonics. It is commonly believed that a topological nontrivial phase would turn into a trivial phase where the transport vanishes under the effect of Anderson localization. Recent studies predict a counterintuitive result, that adding disorder to the trivial band structure triggers the emergence of protected edge states, the so-called topological Anderson phase. Here, we experimentally observe such a topological Anderson phase in a CMOS-compatible nanophotonic circuit, which implements the Su-Schrieffer-Heeger (SSH) model with incommensurate disorder in the intercell coupling amplitudes. The existence of the Anderson phase is verified by the spectral method, based on the continuous detection of the nanoscale light dynamics at the edge. Our results demonstrate the inverse transition between distinct topological phases in the presence of disorder, as well as offering a single-shot measurement technique to study the light dynamics in nanophotonic systems.

DOI: 10.1103/PhysRevResearch.4.033222

I. INTRODUCTION

Over the last decade, the field of topological photonics has witnessed tremendous developments [1–4]. Inspired by topological physics of charged electrons in condensed matter, the topological concepts in photonics have emerged from the discovery of topological phases [5,6] that have been subsequently studied in various systems [7–16]. Photonic topological phases possess intriguing light-guiding behavior from edge states which display inherent robustness against disorder. Studying the topological properties of photonic systems enables a deeper understanding of light dynamics and provides tools for designing photonic systems [17–19], such as light sources [20–25], and robust quantum circuits [26–30] with great prospects.

Recently, the role of disorder has been reevaluated due to the discovery of the topological Anderson phase (TAP) [31–38]. Unlike an ordinary Anderson insulator, where transport is suppressed with increasing disorder strength, the emergence of a TAP is reversely driven by disorder, implying a transition from a trivial to a nontrivial topological phase. Such a TAP has been recently experimentally observed in two-dimensional photonic systems [39,40] as well as one-dimensional disordered atomic wires [41]. Observation of all features of the TAP phase remains elusive. For example, the larger Anderson localization length in two-dimensional systems makes it challenging to observe their bulk localization. It is still debatable whether different types of disorder may prevent the TAP from forming [42–44]. For instance, correlated disorder [43] and incommensurate disorder [44] predict opposite phenomena.

Here, we report on the experimental observation of the TAP in a one-dimensional Su-Schrieffer-Heeger (SSH) lattice [45] with incommensurate disorder. The integrated photonics platform offers precise engineering of the SSH model implementation [4], the lattice is inscribed in a nanophotnic chip with complementary metal-oxide-semiconductor (CMOS) compatible fabrication technology [46]. A spectral method is adopted to verify the zero-energy edge modes with achievable one-shot detection. The light dynamics at the edge is retrieved from our proposed loss-induced scattering approach (LISA) with high fidelity. Our results provide experimental proof of TAP induced by quasiperiodic disorder and serve as a tool to analyze the light dynamics, even with disorder present in a lattice.

*junga@kth.se
†elshaari@kth.se

II. QUASI-PERIODIC SSH MODEL

Conceptually, the SSH model is the simplest system that can exhibit topological trivial and nontrivial phases. These two distinct phases, which are characterized by the winding

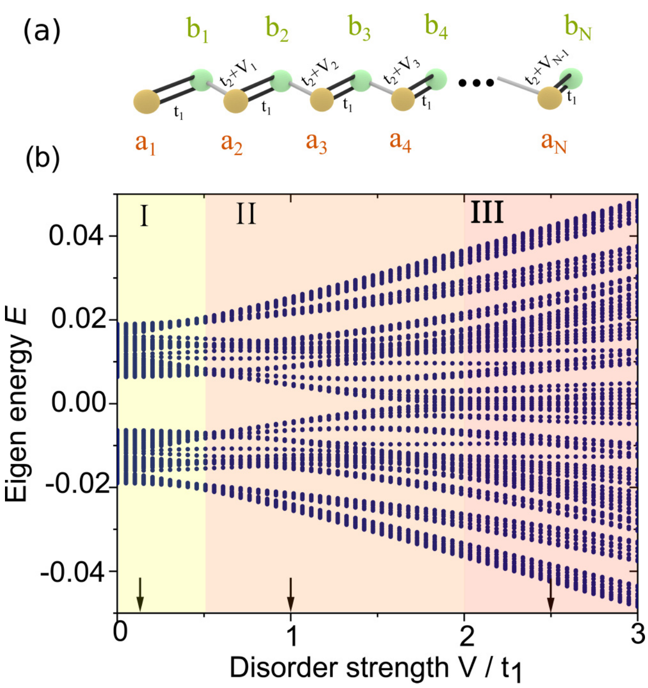

FIG. 1. (a) Schematic of an SSH lattice with intracell and intercell coupling amplitudes t_1 and t_2, respectively. At no disorder, the lattice satisfies $t_1 > t_2$ condition, resulting in a band gap in the energy spectrum with topologically trivial states in the upper and lower energy bands. The intracell coupling is modulated through an incommensurate disorder of strength V. The disorder follows a sinusoidal function with an irrational number α for the period, which is the ratio between two Fibonacci numbers. (b) Energy spectrum E of the disordered SSH lattice as a function of the disorder strength V/t_1. Higher disorder strength forces the system to go through a topological phase transition, with closing of the band gap at $V/t_1 > 2$, and the appearance of zero-energy topologically nontrivial states with nonzero generalized winding number Q.

number W, can be tuned by controlling the ratio between the intracell and intercell coupling amplitudes. As schematically shown in Fig. 1(a), the lattice can be described by the following Hamiltonian:

$$H = \sum_n (t_1 a_n^\dagger b_n + t_2 b_n^\dagger a_{n+1}) + \text{H.c.} \tag{1}$$

Here, $a_n^\dagger(a_{n+1})$ and $b_n^\dagger(b_n)$ are the creation (annihilation) operators at the corresponding sites in the unit cell with different coupling amplitudes, and $t_1(t_2)$ represents the intracell (intercell) coupling strengths. In the integrated waveguide system, the coupling amplitude is determined by the gap between adjacent waveguides [47].

In the standard SSH model, if $t_1 < t_2$, the dimerized-type chain enables topological nontrivial phases with winding number $W = 1$, while for $t_1 > t_2$, $W = 0$. Here, our system starts in a topologically trivial phase $t_1 > t_2$, with fixed value of intracell coupling t_1. Incommensurate disorder is added to the system through the intercell coupling $t_2 = t_2 + V_n$. The exact expression of this disorder is governed by the formula

$$V_n = V\cos(2\pi\alpha n), \quad \alpha = \frac{\sqrt{5}-1}{2}. \tag{2}$$

With the incommensurate disorder added to the intercell bonds, we further calculate the energy spectrum E of this modulated SSH lattice versus disorder strength V/t_1. In our calculation, we set the waveguide number n as 1000, and the coupling amplitude $t_1 = 2t_2$. As shown in Fig. 1(b), the energy spectrum E is symmetric with respect to $E = 0$ due to chiral symmetry, and as the ratio V/t_1 is increased, two nearly degenerate zero-energy modes appear at $V > 2t_1$, check the Appendix for more details about different regimes in the energy spectrum. In our experiment, three values of V are selected, namely, $V = 0.2t_1$, $V = t_1$, and $V = 2.5t_1$, to explore the effect of disorder. As indicated by the energy spectrum in Fig. 1(b), the most intriguing phase transition happens between regions II and III, where the closing band gap leads to the appearance of zero-energy eigenmodes.

Analytically, for a disordered SSH lattice with chiral symmetry, we can introduce the generalized winding number Q, a topological number to identify the TAP. Q can be expressed as

$$Q = \tfrac{1}{2}(1 - Q'), \tag{3}$$

where

$$Q' = \text{sign}\left\{\prod_n t_1^2 - \prod_n (t_2 + V_n)^2\right\}. \tag{4}$$

A detailed theoretical derivation [38,48] leads to $Q' = 1$ for $V < 2t_1$, and $Q' = -1$ for $V > 2t_1$. This result clearly shows that $V = 2t_1$ is the phase transition point in TAP, and the existence of a zero-energy mode can be characterized by the topological number $Q = 1$ $(Q' = -1)$ (see Appendix for numerical calculation of Q in a disordered SSH lattice).

Experimentally, it is challenging to directly probe the topological number Q [49]. The bulk-edge correspondence is typically used to verify the existence of nontrivial topologically protected states in disorder-free lattice through imaging of edge-localized light transmission. This approach, unfortunately, cannot be extended to the SSH lattices with disorder, even when the disorder strength is smaller than the critical value of $V < 2t_1$ [38]. Exciting the disordered lattice at the edge leads to light dynamics localized at the edge, which cannot be regarded as a signature of the TAP. Instead, spectral analysis of the light dynamics near the edge of the lattice can provide a clear signature of the Anderson transition as proposed in Refs. [38,50]. Measuring the autocorrelation function of a lattice site as the system evolves can reveal its energy spectrum through the Wiener-Khinchin theorem:

$$C(E) = \frac{1}{L}\int_0^L dz a_1^*(0) a_1(z) \exp(iEz). \tag{5}$$

Here, $a_1(z)$ is the evolution of the light amplitude in the excitation waveguide and L is the propagation length. Note that $C(E)$ will be simplified to the sampled Fourier transform of $a_1(z)$ if we only have the single-site input excitation. The spectral analysis is a feasible method to experimentally verify the existence of a zero-energy mode, with a suitable chosen sampling rate.

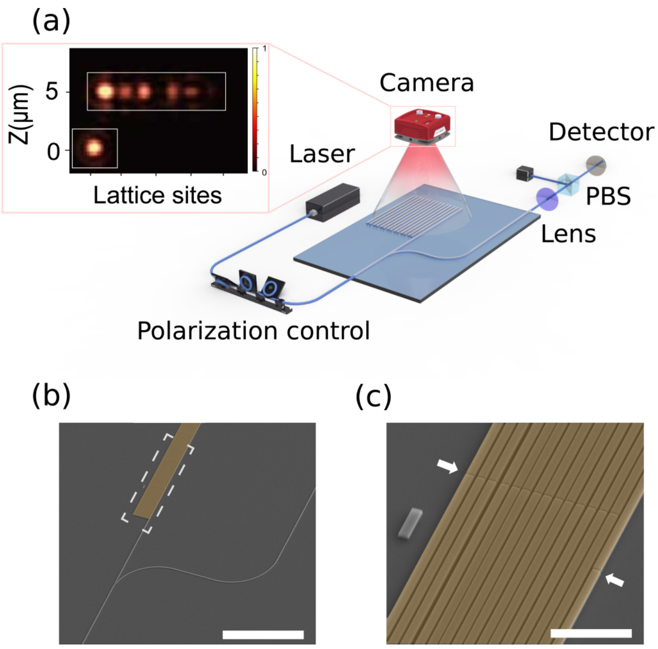

FIG. 2. (a) Schematic of the experimental setup. The source consists of a continuous wave 795 nm laser. A fiber coupled polarization controller is used to excite the fundamental TE mode of the edge-waveguide in the SSH photonic lattice. The output of the chip is free-space coupled to an optical power meter through a polarizing beam splitter to monitor the excited polarization in the SSH lattice. The light scattered from the induced scattering sites is top-imaged using a microscope system equipped with a CCD camera. Inset: LISA top image to measure the light dynamics in the SSH photonic lattice. Intensity samples are taken every 25 μm. In total, 700 μm propagation length was considered for the evaluation of the results, with the full data-set included in the Appendix. (b) SEM image of integrated photonic circuit, where the input waveguide branches to the SSH lattice and a reference port. (c) Magnified SEM image of the LISA structure to sample light intensity in a single nanowaveguide. The white arrows indicate the location of LISA structures. The scale bars in (b) and (c) correspond to lengths of 50 μm and 5 μm, respectively.

III. EXPERIMENTAL OBSERVATION OF ANDERSON PHASE

The schematic of the experimental setup is shown in Fig. 2(a). We fabricate our topological photonic lattice using a Si_3N_4-based platform. The coupling amplitude of the waveguide is numerically simulated, see the Appendix for more details related to the lattice design, simulation, and fabrication. The waveguides' spacing in the lattice is selected according to the coupling amplitude modulation between lattice sites. In total, there are 15 waveguides in the SSH lattice. The usage of an odd number of waveguides in our lattice does not change the physics through introducing a defect, as the waveguide at the opposite end of the device is far from the excitation site. The number of lattice sites is chosen based on numerical simulations, allowing for light localization at the edge with a finite number of lattice sites, at the same time providing a feasible experimental implementation. We use a coherent laser source centered at 795 nm to excite the lattice. The light signal is coupled to the nanophotonic chip with a lensed fiber, mounted on a 5-axis nano-positioning stage. The transverse electric (TE) mode of the waveguide is selectively excited using a fiber-coupled 3-paddle polarization-controller at the input and a polarizing beam splitter at the output. The input waveguide is split into two paths by an on-chip Y-splitter [see Fig. 2(b)]. One path is directed to the input port of the modulated SSH lattice. The evolution pattern of the light along the propagation direction is top imaged by a 50X long working distance objective and then characterized via a charge-coupled device (CCD) camera. The other path of the Y splitter serves as a monitor for the coupling efficiency during the measurement, where the output beam is collimated with a 100X objective and then detected by a silicon-based optical power meter.

The dimension of the Si_3N_4 waveguide is 600 nm $\times$ 250 nm, with spacing between waveguides on the order of 150 nm, so using an optical microscope to identify and analyze the light in individual waveguides is technically challenging. Here, we propose a method that enables monitoring the nanoscale light dynamics using a LISA. The central idea of the LISA is to deliberately introduce a periodic gap in the excitation waveguide. This loss structure scatters a small ratio of the light transmitted in the nanowaveguide at a specific location, enabling its collection and imaging. To compensate the loss in the excitation waveguide and preserve the state fidelity, we introduce a uniform loss in the remaining lattice sites after 5 μm distance from the excitation waveguide scattering site, which is much smaller than the coupling lengths in our system (see Appendix). In such a way, the total loss introduced to the photonic system can be considered near uniform, which has little effect on the light dynamics [51]. Detailed analysis of the scattering loss from the LISA and the state fidelity compared to a lossless lattice can be found in the Appendix. A scanning electron microscope (SEM) image of the LISA structure is shown in Fig. 2(c). The inset of Fig. 2(a) shows top imaging of a LISA structure to sample the intensity at the edge lattice site, with compensating structures in the remaining waveguides. We fabricate 32 LISA structures in the excitation waveguide with a sampling period of 25 μm.

The full data set of LISA top images are included in the Appendix. We study three groups of disorder strengths: $V/t_1 =$ 0.2 and 1 correspond to the trivial states with zero topological number, while $V/t_1 = 2.5$ corresponds to a topologically nontrivial state with nonzero generalized winding number Q. The three disorder strengths reflect the three operating regimes shown in Fig. 1(b). In the excitation waveguide of the SSH lattice, scattered light spots can be clearly observed using top imaging [Fig. 2(a) inset], the intensity for different scattering sites along the propagation direction is recorded using a CCD camera.

To construct the energy spectrum of the propagating state, both field amplitude and phase information are needed. The phase information is typically lost in an intensity-based imaging experiment. We follow the procedure highlighted in Ref. [38] to retrieve the full amplitude in the excitation site: (a) excite the edge waveguide, (b) monitor the intensity of light evolution using the fabricated sampling structures, and (c) calculate the field evolution by taking the square root of intensity, with an appropriate sign.

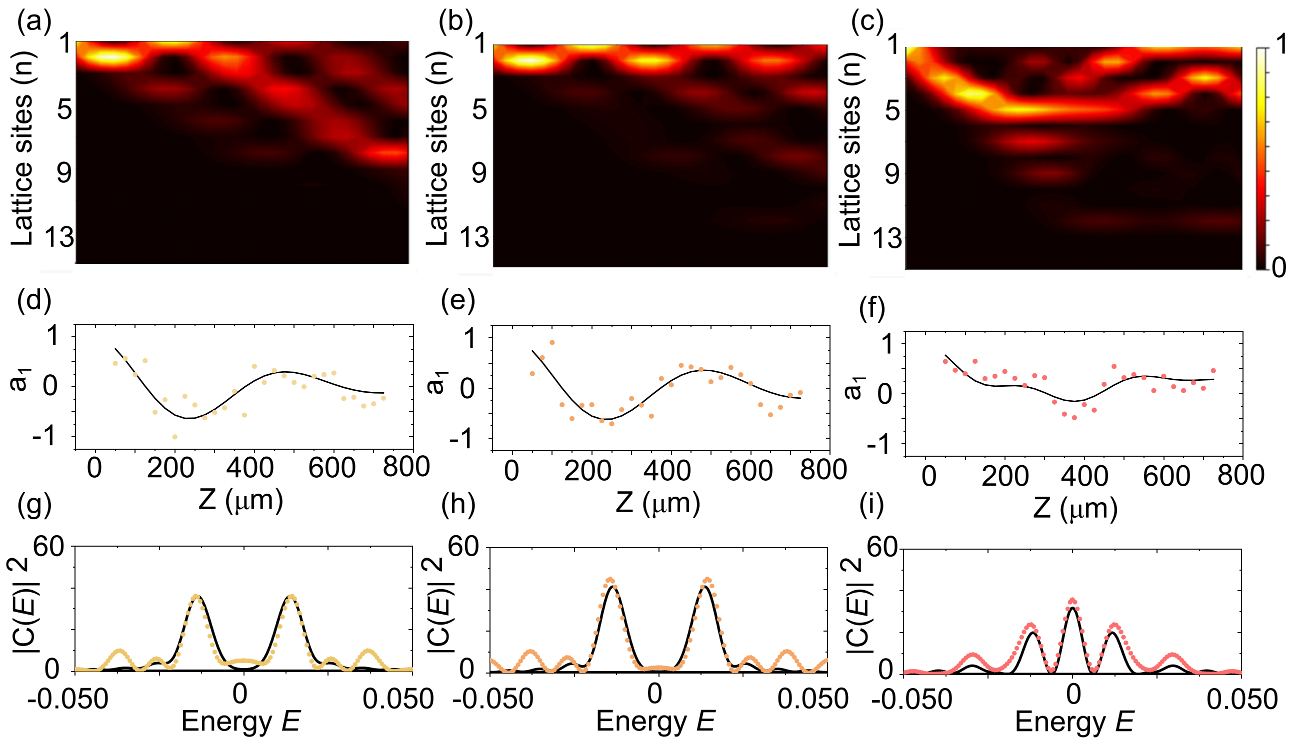

FIG. 3. (a)–(c) Simulated light-intensity evolution in each waveguide of an SSH photonic lattice for three disorder strengths $V/t_1 = 0.2$, 1.0 and 2.5, respectively. (d)–(f) show the experimentally measured field amplitude in the edge-waveguide reconstructed from the intensity measurement. The solid lines correspond to the simulated field evolution for different disorder strengths. (g)–(i) show experimentally measured energy-spectrum of the edge lattice-site. The solid lines show the simulated energy spectrum, showing good agreement with the experimentally measured data. The spectral method clearly reveals the presence of a zero-energy peak at higher disorder strength $V/t_1 > 2$, corresponding to a non-zero generalized winding number of the Hamiltonian. All the presented results are fitted using only one free-parameter corresponding to a waveguide loss including the loss elements of 10.6 dB/mm.

The phase will experience a π jump when the light is fully reflected at the boundary of the lattice. This simplifies the task of calculating the energy considerably, with no need of applying a sophisticated technique for phase retrieval [52], since two binary phase values are involved, namely, 0 or π. The sign of the field can be determined through modeling the fabricated lattices. The phase jump occurs when the light is reflected by the boundary of the lattice; more details about the sign of the field amplitude in the edge site are given in the Appendix. Owing to the robustness of the topological circuits, the exact gaps and coupling amplitudes in the design of the fabricated circuits are used in the model, with only the waveguide propagation loss as a free parameter. The light intensity samples are taken at 25 μm sampling period, matching the fabricated structures. Figures 3(a)–3(c) show the simulated dynamics of an edge-excited lattice for three disorder strengths $V/t_1 = 0.2$, 1.0, and 2.5. The light dynamics show oscillation near the edge waveguide, thus considering edge localization alone cannot provide a clear signature of the TAP.

Figures 3(d)–3(f) show the experimental and the simulated field amplitude for the three disorder strengths. The effect of including the LISA elements is considered in the field amplitude evolution simulation to match the experimental data as the excited-state evolves in the lattice. The experimental field amplitudes show good agreement with the simulated SSH lattices, the main source of deviation comes from the scattering site (50 nm gap) transmission efficiency. Characterizations of the scattering-elements and fabrication accuracy are discussed in the Appendix. The experimental and simulated energy spectrum $|C(E)|^2$ for the three selected disorder strengths are shown in Figs. 3(g)–3(i). An energy gap is open in the system for disorder strength ($V < 2t_1$) [see Fig. 1(b)], resulting in no zero-energy state. This is represented in Figs. 3(g) and 3(h) with $|C(E)|^2$ not displaying a marked peak centered around $E = 0$. Above the critical point of $V = 2t_1$, the energy spectrum shows a clear zero-energy peak indicating the TAP at such disorder strengths. The demonstrated results show that in an SSH model with quasiperiodic disorder, the Anderson phase transition occurs. The transition is associated with a nonvanishing topological number Q, which counts the number of topologically protected edge states [38,53]. Q takes a value of 0 for $V < 2t_1$ and 1 for $V > 2t_1$. The spectral measurements in Fig. 3 demonstrate that such a transition with nonzero topological number can be discovered through detecting the zero-energy peak in the spectrum of the edge state autocorrelation function. To further prove the robustness of the experiment, we in total measured 18 devices, 6 for each operating regime in Fig. 1; the results are shown in Fig. 4. Even for devices on various fabrication runs, a consistent Anderson phase transition can be observed. The transition of

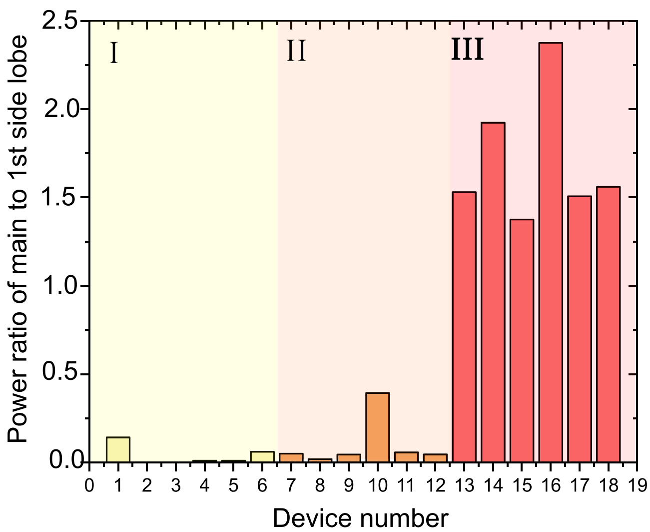

FIG. 4. Robustness of topological transition. Ratio of the spectral components of the zero energy state to the first excited state, at different disorder strengths $V/t_1 = 0.2$, $V/t_1 = 1$, and $V/t_1 = 2.5$. In total, 18 devices were tested, six devices for each operating regimes in Fig. 1. A consistent Anderson transition can be observed, even for devices on different fabrication runs. The discrete transition to the nonzero generalized winding number Q between the trivial and nontrivial regimes provides robustness against local disorders due to fabrication, with no statistical overlap between the two regimes of trivial and nontrivial states.

the generalized winding number Q between the trivial and nontrivial regimes gives resilience against local disruptions due to fabrication. The Appendix contains the whole data set of all the devices' measured energy spectra.

IV. CONCLUSION

Topological photonic insulators show resilience to disorder through edge states that are not susceptible to backscattering, as they are protected on a topological level. With sufficient disorder, these systems become topologically trivial and all transport ceases to exist in line with Anderson localization [54]. It is surprising that the opposite can also be true [31,39,40]. The experiment presented here demonstrates TAP on a nanophotonic device that implements the SSH model with incommensurate disorders in the intercell coupling amplitudes. The Anderson phase transition is validated using spectral analysis of the zero-energy edge state and by monitoring the light dynamics, based on sampling the nanoscale light intensity in the SSH lattice. Our results demonstrate the complex relationship between topology and disorder. The ability to control the disorder strength provides an important tool in combining the ideas from random lasers with disordered topological systems. The demonstrated platform is compatible with standard CMOS fabrication processes, enabling hybrid integration with III-V and two-dimensional materials [55] to explore the physics of Anderson topological phase transitions in the presence of interaction with quantum emitters and nonlinear media.

ACKNOWLEDGMENTS

A.W.E acknowledges support from the Knut and Alice Wallenberg (KAW) Foundation through the Wallenberg Centre for Quantum Technology (WACQT), Swedish Research Council (VR) Starting Grant No. 2016-03905), and Vinnova quantum kick-start Project No. 2021. S.S. acknowledges support from VR Starting Grant No. 2019-04821. V.Z. acknowledges support from the KAW and VR. D.A.S acknowledges support by the Australian Research Council (Grant No. DE190100430). D.L. acknowledges support from the National Research Foundation, Prime Minister's Office, Singapore and the Ministry of Education, Singapore under the Research Centres of Excellence Programme.

APPENDIX A: SU-SCHRIEFFER-HEEGER DISORDERED PHOTONIC LATTICE

The dynamics in our system is described by a one-dimensional Hamiltonian with real hopping amplitudes between different lattice sites [38],

$$\hat{H} = \sum_n (t_1 a_n^\dagger b_n + (t_2 + V\cos(2\pi\alpha n)) b_n^\dagger a_{n+1}) + \text{H.c.}, \tag{A1}$$

where $a_n^\dagger(a_{n+1})$ and $b_n^\dagger(b_n)$ are the creation (annihilation) operators at the corresponding sites and $\alpha = \frac{\sqrt{5}-1}{2}$ is the ratio between two Fibonacci numbers $\alpha = q_{n-1}/q_n$ for the sequence $q_0 = 0$, $q_1 = 1$, $q_{n+1} = q_n + q_{n-1}$. The real constants t_1 and t_2 are nearest-neighbor hopping amplitudes between the lattice sites. V is a real-valued parameter to control the disorder-strength in the lattice. At the limit of $V = 0$, our system reduces to the standard SSH model with two topologically distinct phases [45]. For $t_1 > t_2$, the system has a topologically trivial band structure with zero winding number, while in the case of $t_1 < t_2$ the system has a nontrivial topological band structure with a nonzero winding number. While it is possible to obtain closed form solutions for the winding number and dispersion relation in disorder-free lattice [2], we use numerical methods to calculate a generalized winding number Q in our disordered system [38,53]:

$$Q = \frac{1}{2}\left(1 - \text{sign}\left\{\prod_n t_1^2 - \prod_n (t_2 + V_n)^2\right\}\right). \tag{A2}$$

Figure 5(a) shows the generalized winding number for a disordered SSH lattice for different disorder strengths V/t_1. The simulation uses a 1000-site lattice, with the same coupling parameters as the fabricated lattice in the main text ($t_1 = 0.0126\ \mu\text{m}^{-1}$ and $t_2 = 0.0063\ \mu\text{m}^{-1}$). The system exhibits a topological phase transition at $V/t_1 = 2$, between regions II and III of Fig. 1 in the main text. To further highlight the properties of different operating regimes in the energy band diagram, we calculate the inverse participation ratio (IPR), which provides a means of characterizing the localization of different eigenstates in the system [50],

$$I_l = \frac{\sum_n \left(\left|a_n^{(l)}\right|^4 + \left|b_n^{(l)}\right|^4\right)}{\left(\sum_n \left(\left|a_n^{(l)}\right|^2 + \left|b_n^{(l)}\right|^2\right)\right)^2}, \tag{A3}$$

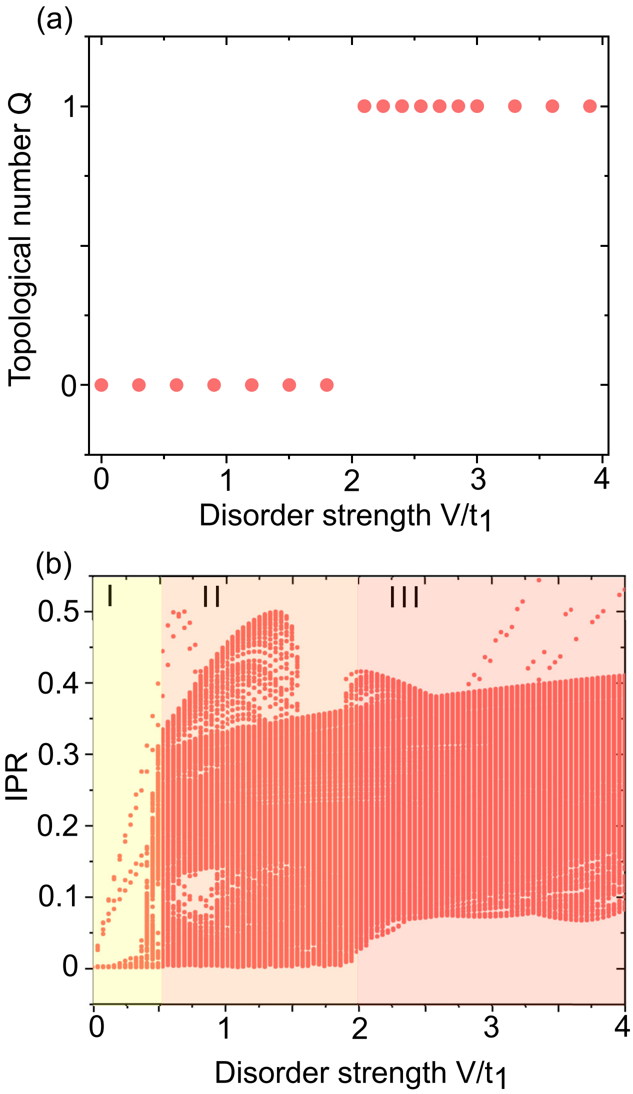

FIG. 5. (a) Topological number Q calculated for a SSH lattice with 1000 lattice sites versus incommensurate disorder strength V/t_1. The system exhibits a topological phase transition at $V/t_1 = 2$, corresponding to a nonzero winding number for $V/t_1 > 2$. (b) Numerically computed IPR of the eigenstates versus disorder strength. The simulation uses the same physical device parameters as in the main text, with a topologically trivial phase at $t_1 = 2t_2$ and zero disorder $V = 0$. At disorder strength $V/t_1 < 0.5$, the majority of the eigenstates are delocalized. At disorder strength $V/t_1 > 0.5$, many of the eigenstates become localized as indicated by the larger IPR, but some eigenstates still possess an IPR value of zero, indicating full delocalization. At higher disorder strength $V/t_1 > 2.0$, all the eigenstates get localized.

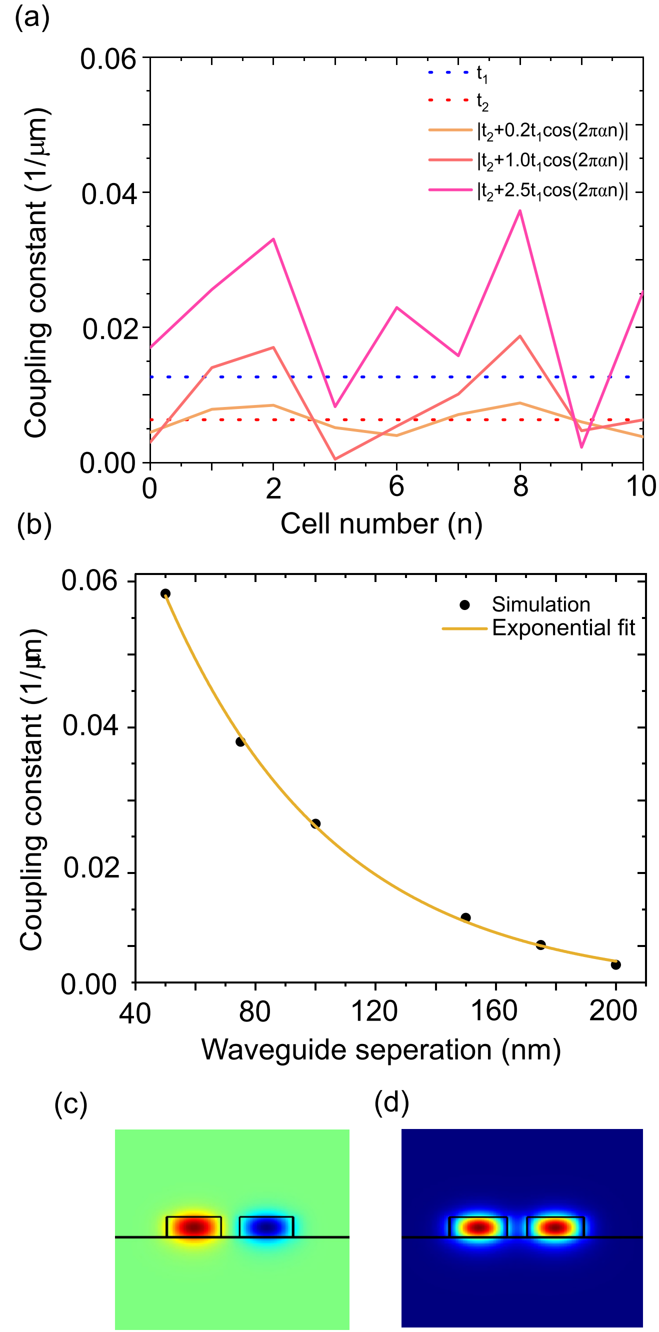

FIG. 6. (a) Coupling amplitude of the intracell t_1 bond, intercell t_2 bond, and three levels of quasiperiodic disorder strength V. (b) Coupling strength per micrometer between two waveguides for different spacing between them. The simulated data is fitted with an exponential function with a decay constant of 0.0276 μm^{-1}. Panel (c) shows the real x component of the electric field for the TE (transverse-electric field) even and odd modes supported by a waveguide coupler.

where l is the eigenstate index and the sum is carried over all lattice sites. Figure 5(b) shows the calculated IPR for a disordered system with 1000 lattice sites; three regions are identified at different disorder strengths V/t_1. Region I: The majority of the eigenstates are delocalized as indicated by IPR values close to zero. Region II: The majority of eigenstates are localized. Region III: All the eigenstates are localized as indicated by IPR > 0.

APPENDIX B: CHIP DESIGN PARAMETERS

Following the guidelines provided by the theoretical model highlighted earlier, we select three quasiperiodic disorder strengths V corresponding to the three regions in Fig. 5. Figure 6(a) shows the coupling amplitudes in the inter- and intradimer bonds for three V values, where $\alpha = (\sqrt{5} - 1)/2$. The system is initially in the trivial state and is driven to a nontrivial, topologically protected edge state at higher disorder strength. We design a photonic chip based on silicon nitride (Si_3N_4) technology [56–58] to explore the physics of the model at different operating conditions. The Si_3N_4 thickness is 250 nm and the waveguide width is 600 nm. Each lattice site in the SSH model will consist of a single Si_3N_4 waveguide, with SiO_2 and air as bottom and top cladding, respectively. The air cladding and the unequal waveguide dimensions in the x and y directions lift the degeneracy between the two orthogonal modes supported in a single waveguide [57], namely, the TE and transverse magnetic (TM) modes. The chosen waveguide dimensions and cladding results in the TM mode are weakly localized, so we focus on the TE modes in the experiment. To tune the coupling strength between the lattice sites, we modify the interdimer waveguide spacing. The coupling strength per unit distance between two waveguides has an exponential relation with the waveguide spacing [59], as shown in Fig. 6(b). The coupling constants are calculated from the difference of the effective refractive indices of the odd and even modes in a two-waveguide cell ($C = \pi\Delta n/\lambda_0$). Figure 6(c) shows the even and odd modes in a dimer of two waveguides, where the odd mode has a slightly higher effective refractive index than the even mode.

The use of the Fibonacci number in the paper is not unique, other irrational numbers would suffice. However, our choice of the ratio has important experimental significance. The coupling constant has an exponential relationship with the gap between the waveguides as shown in Fig. 6(b). The electron beam resist used in the fabrication process, m-aN 2403, spins to a thickness of 300 nm at 4000 rpm. This sets a limitation on the aspect ratio of the fabricated structures (thickness of silicon nitride is 250 nm). We limited the gaps in our structure to be more than 80 nm for the 15 waveguide SSH lattices we fabricated. The choice of $\alpha = (\sqrt{5} - 1)/2$ satisfies the criteria described for the modulated values of the coupling t_2.

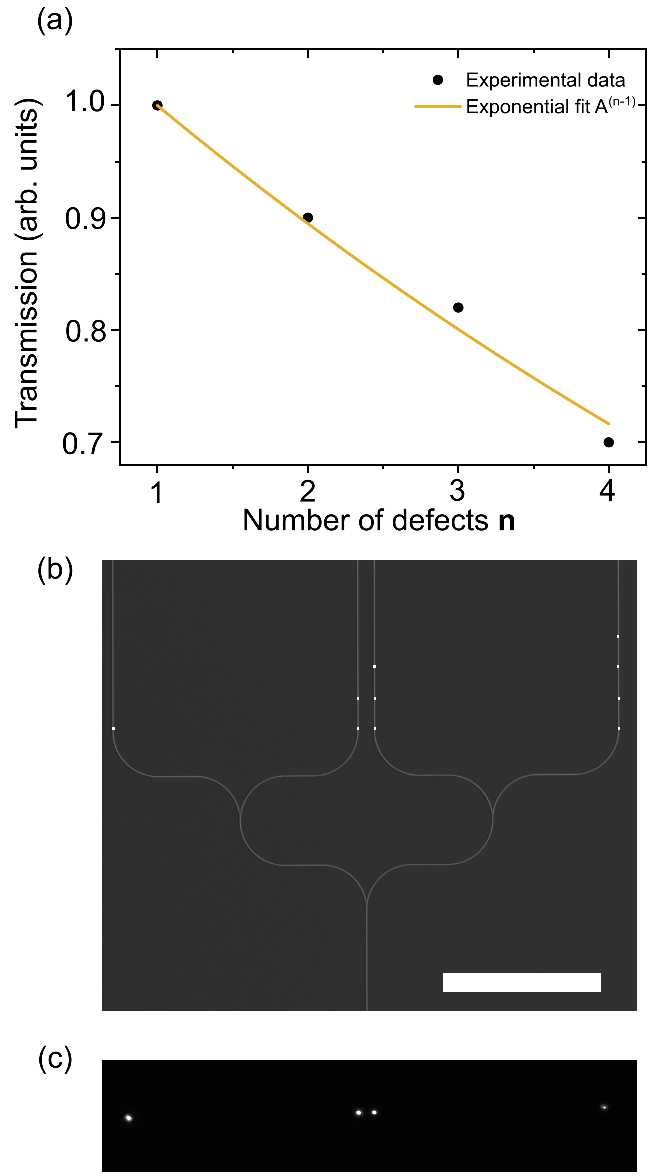

FIG. 7. (a) Waveguide transmission as a function of the number of defects. Experimental data is fitted with an exponential function A^{n-1}, where A is 0.95 and n is the number of defects. (b) Scanning electron microscope image of the fabricated device with three Y splitters leading to four waveguides with different defect numbers $n = 1, 2, 3$, and 4. The defects are highlighted by white markers, the scale bar corresponds to a length of 100 μm. (c) Top image of the chip side-facet. The light spots correspond to transmission through the waveguides with different number of defects.

APPENDIX C: SSH LATTICE FABRICATION AND CHARACTERIZATION

The topological photonic circuits are realized using commercial Si wafers covered with 3.3 μm SiO_2 and 250 nm Si_3N_4. The waveguide structures are fabricated by electron beam lithography (negative-tone resist; 50 kV electron acceleration voltage) and subsequent pattern transfer via dry etching of Si_3N_4 (CF_4-based reactive ion etching). Proximity correction is performed to mitigate the effect of backscattered electrons in dense waveguide array patterns. Eventually, the samples are cleaved to allow for optical coupling to the Si_3N_4 waveguide side facets. Note that no additional cladding layers are used in the presented experiments.

In modeling the light dynamics, only a single free parameter in fitting the experimental results (Fig. 4 in the main text) is used; it corresponds to the waveguide field attenuation factor of 0.95 per scattering site. All other parameters, such as the coupling constants and the disorder strength, are directly applied from the theoretical model and chip design parameters. To accurately measure the field transmission constant as a function of the defects, a photonic chip with a single input and four outputs connected by three beam splitters is fabricated. The four waveguide branches host $n = 1, 2, 3$, and 4 defects, respectively. Figure 7(a) shows the transmission in the waveguides as a function of the number of defects, fitted with an exponential function A^{n-1}, where A is 0.95 and n is the number of defects. Figure 7(b) shows a SEM image of the fabricated chip, where defects are highlighted by white markers. Figure 7(c) shows a captured intensity image of the light transmitted to the facet of the chip. The experimentally

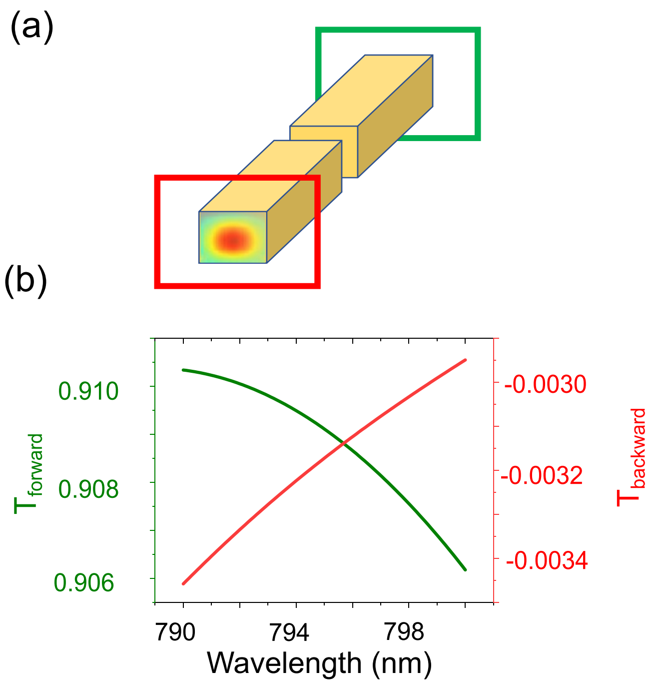

FIG. 8. (a) Schematic of the simulated structure, with two monitors in the forward and backward directions highlighted by green and red rectangles, respectively. (b) Forward and backward transmission and reflection coefficients to the guided modes in the waveguide.

measured field loss is 5%, which is slightly higher than the field-loss factor used in the model of 3%. The deviation is attributed to the accuracy in achieving consistent 50 nm gaps in the fabricated intensity sampling structures. The electron beam resist thickness is approximately 300 nm, which sets a limitation on etching high aspect-ratio structures in 250-nm-thick Si_3N_4. The limitation in the gap fabrication is linked to an added noise in the top intensity measurement data, presented in the main paper.

APPENDIX D: TRANSMISSION AND REFLECTION COEFFICIENTS

The loss in each LISA structure can be decomposed into two parts: (i) light coupled to unguided modes, i.e., top and bottom scattering, a part of which we can detect using a CCD camera in our setup, and (ii) back-reflected light, which is coupled to the single mode waveguide in the counterpropagating direction. This back-reflection is typically very small, which has nearly no effect on the evolution forward.

To confirm this assumption, we performed three-dimensional finite-difference time-domain simulations. Figure 8(a) shows the structure of the simulated device whose parameters correspond to the experimental parameters of the chip. The bottom cladding is silicon oxide, while the top cladding is air. The LISA structure represents a gap of 50 nm. To accurately simulate the light dynamics accompanied by scattering, we adopted an adaptive mesh configuration with a mesh precision of 5 nm at the LISA structure. Two monitors, denoted by the red and green frames, are utilized to record the transmission and reflection of the single TE mode supported by the waveguide. The results are shown in Fig. 8(b).

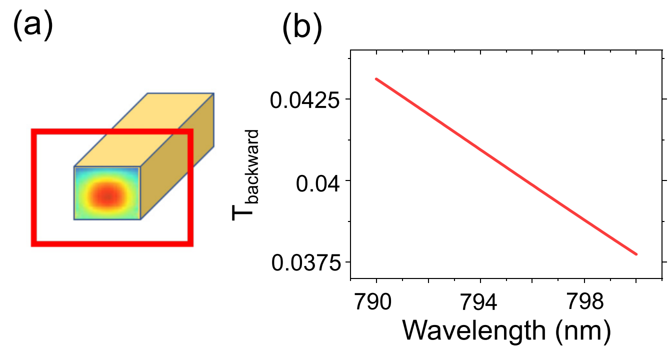

FIG. 9. (a) Schematic of the simulated structure, with one monitor to measure the backreflected light to the guided mode from the end facet. (b) Computed reflection coefficient from the facet to the guided mode in the waveguide.

The coupling of light to the backward propagating mode is more than 300 times, two orders of magnitude, smaller than the transmission forward. Moreover, the calculated intensity transmission coefficient shows excellent agreement with the measured experimental data. The simulation further stresses a very minor impact of the backward propagating modes on the overall device performance, as the contribution from subsequent LISA structures decreases exponentially under nonresonant and phase matching conditions.

We also consider the back reflection from the end facet of the waveguide. Although at first glance the reflection in such nanosized waveguides might seem to be higher than that in the laser-written waveguides or optical fibers, this is not the case. When an optical fiber is terminated, the return loss is typically 3%, which originates from a mismatch between the effective refractive index of the mode and the refractive index of the air termination. The effective refractive index of the nanosized waveguide $n_{\mathrm{eff}} \approx 1.6$ is comparable to that of an optical fiber, which is lower than the bulk material index of silicon nitride. We simulated our structure as illustrated in Fig. 9(a): the waveguide is terminated by air, and the back reflected light to the guided mode is measured. The line plot in Fig. 9(b) shows that only 4% of the forward propagating mode couples to the backward mode due to facet reflection. Such facet reflection value is rather common for all the integrated platforms (fs laser writing silica chip or CMOS compatible nano photonic chips) [26,60].

APPENDIX E: EXTENDED TIGHT-BINDING MODEL

To account for backscattering at slit defects in the waveguides, we extend the conventional tight-binding model for the wave field evolving in the forward direction by introducing its coupling to the backward propagating modes. In this way, light dynamics in the waveguide array can be described by two SSH-like subsystems, a_n and b_n, with a numerically estimated coupling of 0.3 percent between the two at each LISA structure.

The forward evolution in the lattice is governed by the equations

$$\frac{da_n}{dz} = -\mathrm{i}(\beta a_n + t_1 a_{n-1} + t_2 a_{n+1}), \qquad \text{(E1)}$$

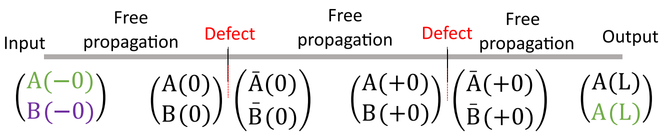

FIG. 10. Schematic of propagation line with forward A and backward B subsystems coupled at LISA defects.

where $t_{1,2}$ are the coupling coefficients between the waveguides, β is the propagation constant in the waveguide. The auxiliary equations capture the effect of coupling to the backward mode as a result of scattering at each LISA defect positioned at Z_m:

$$a_n(Z_m+0) = ta_n(Z_m-0) + r'b_n(Z_m+0). \tag{E2}$$

Similarly, we write equations for the field propagating in the reverse direction caused by back-scattering:

$$\frac{db_n}{dz} = -\mathrm{i}(-\beta b_n + t_1 b_{n-1} + t_2 b_{n+1}), \tag{E3}$$

$$b_n(Z_m-0) = tb_n(Z_m+0) + ra_n(Z_m-0). \tag{E4}$$

The constants in the auxiliary equations are determined from the scattering matrix of the LISA structure that relates the outgoing fields to the incoming ones:

$$\begin{pmatrix} a_n(Z_m+0) \\ b_n(Z_m-0) \end{pmatrix} = \begin{pmatrix} t & r' \\ r & t \end{pmatrix} \begin{pmatrix} a_n(Z_m-0) \\ b_n(Z_m+0) \end{pmatrix}, \tag{E5}$$

where r and r' are the reflection coefficients from the left and right, respectively, and t is the transmission coefficient,

A scheme in Fig. 10 illustrates the field propagation across two LISA structures, which are repeated at equal separations for the total propagation length L of the device. A and B denote the amplitudes in the forward and backward SSH subsystems. The boundary conditions, with the only input in the edge waveguide, imply $A(-0) = (1, 0, \dots 0)^T$ and $B(L) = (0, 0, \dots 0)^T$. To convert the boundary value problem into the initial value problem, we search for the backscattering amplitude $B(-0)$ through the matrix multiplication. We define transfer matrices for repeating segments of free propagation and defect scattering. Parameters of the defect matrix $\widehat{M}_d$ are extracted directly from the FDTD simulation for the fundamental TE mode in a silicon-nitride waveguide with a slit defect, as formulated by Eq. (E5). Then the last interval, comprising free uncoupled propagation at length L_p and a point defect, is described by matrix $\widehat{M}$:

$$\begin{pmatrix} A(L) \\ B(+0) \end{pmatrix} = \begin{pmatrix} e^{-i\hat{H}L_p} & 0 \\ 0 & 1 \end{pmatrix} \widehat{M}_d \begin{pmatrix} 1 & 0 \\ 0 & e^{i\hat{H}_b L_p} \end{pmatrix} \begin{pmatrix} A(+0) \\ B(L) \end{pmatrix}, \tag{E6}$$

$$\begin{pmatrix} A(L) \\ B(+0) \end{pmatrix} \equiv \widehat{M} \begin{pmatrix} A(+0) \\ B(L) \end{pmatrix}, \tag{E7}$$

where we have matrix exponentials, with $\hat{H}$ and $\hat{H}_b$ being matrix Hamiltonians for the forward and backward SSH subsystems. We can sequentially redefine the matrix $\widehat{M}_m$ for the repeating segments to write the amplitude relations in the same way as in Eq. (E7),

$$\begin{pmatrix} A(L) \\ B(0) \end{pmatrix} = \widehat{M}_m \begin{pmatrix} A(0) \\ B(L) \end{pmatrix}. \tag{E8}$$

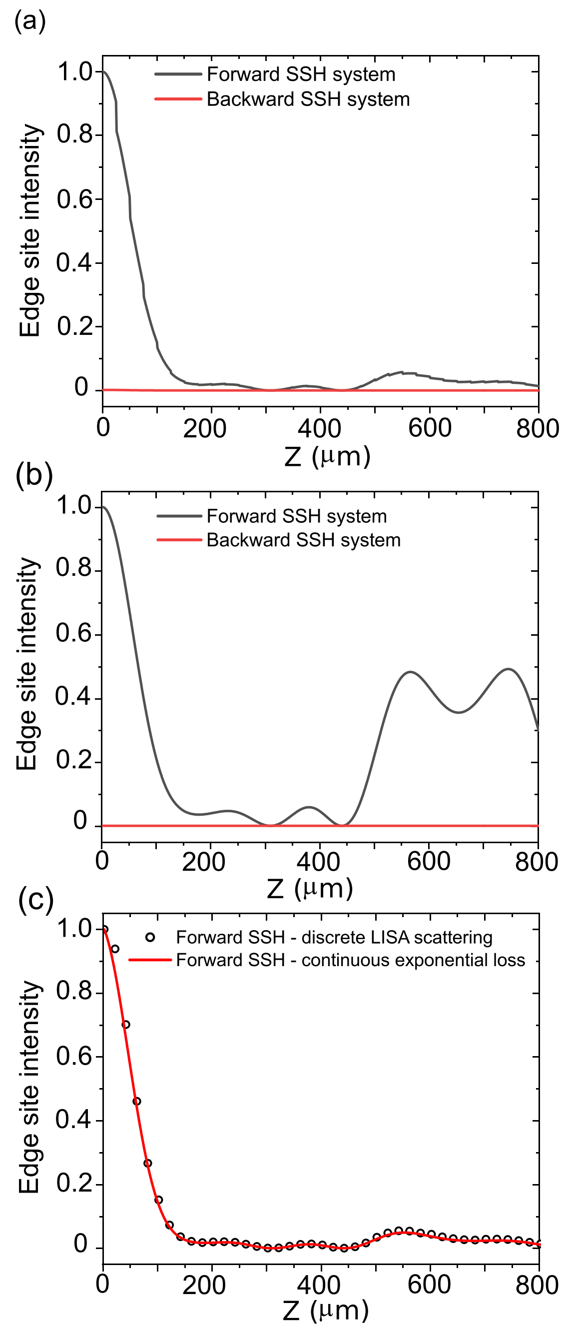

FIG. 11. Effect of scattering on the system performance. (a) Intensity distribution of the forward (black curve) and backward (red curve) modes in the edge waveguide along the propagation direction in arrays with LISA structures equidistantly spaced at 25 μm. (b) Intensity distribution of the forward (black curve) and backward (red curve) modes in the edge waveguide along the propagation direction at the ideal case of no scattering sites. (c) Intensity distribution of the forward modes in the edge waveguide for two cases: LISA structures equidistantly spaced at 25 μm (black dots) and continuous exponential loss with decay factor of 243.725 μm^{-1} (red curve).

The full response of the system is then given by

$$\begin{pmatrix} A(L) \\ B(-0) \end{pmatrix} = \begin{pmatrix} 1 & 0 \\ 0 & e^{i\hat{H}_b L_p} \end{pmatrix} \widehat{M}_m \begin{pmatrix} e^{-i\hat{H}L_p} & 0 \\ 0 & 1 \end{pmatrix} \begin{pmatrix} A(-0) \\ B(L) \end{pmatrix}. \tag{E9}$$

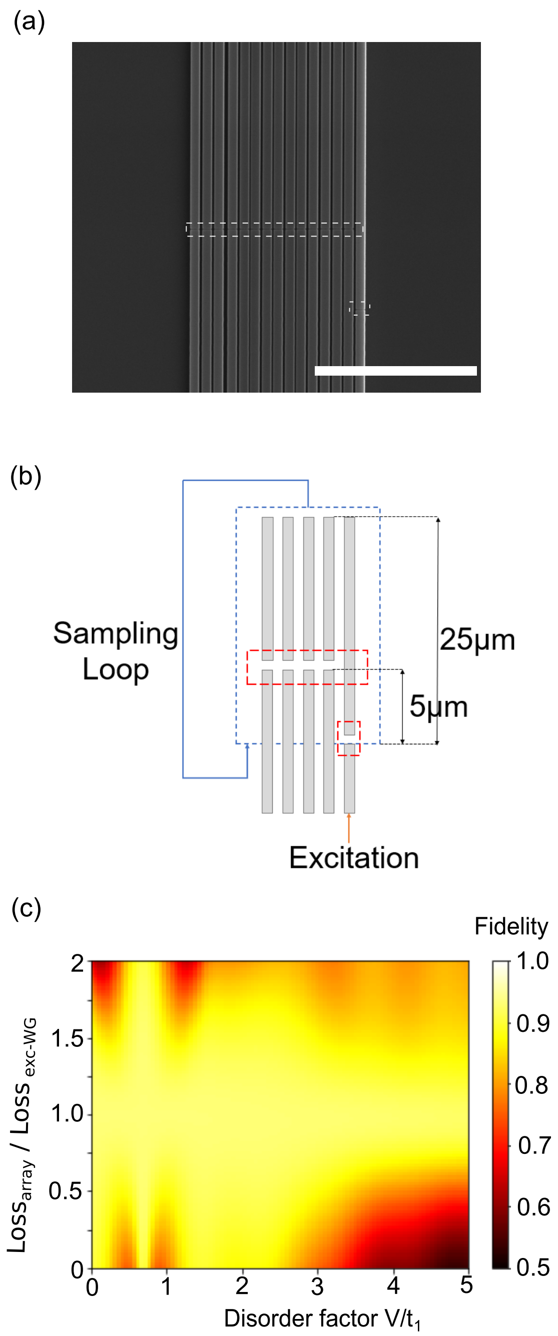

FIG. 12. (a) Scanning electron microscope image of the SSH photonic lattice with additional defects to sample the light intensity in different waveguides. The defects are indicated by white markers, the scale bar corresponds to a length of 10 μm. (b) Unit cell used to calculate the state fidelity as the light propagates in the SSH lattice. The unit cell has a length of 25 μm, the edge-waveguide defect and the line-defect in the remaining lattice sites are located at 0 μm and 5 μm distance from the unit cell edge, respectively. (c) 2D plot of the state fidelity after a propagation length of 800 μm for different disorder strength V/t_1 and ratio between the excitation waveguide loss and the line defect loss.

As soon as $B(-0)$ is found, we may reconstruct the evolution across the system by solving the initial value problem.

Equipped with the theoretical model above, we performed numerical modeling to confirm the negligible effect of the backscattering on the system performance, as visualized in Fig. 11. Figure 11(a) shows the intensity distribution of forward (black curve) and backward (red curve) modes in the edge waveguide along the propagation direction in arrays with 25 μm LISA structures at $V = 2.5t_1$. At the ideal scenario of no scattering sites, the intensity distribution of the forward (black curve) and backward (red curve) modes in the edge waveguide along the propagation direction is shown in Fig. 11(b). To compare the two cases, Fig. 11(c) shows the forward mode intensity distribution in the edge waveguide for two cases: equidistantly spaced LISA structures at 25 μm (black curve) and continuous exponential loss with a decay factor of 243.725 μm^{-1}. We notice from the figures that the coupling to the backward modes is negligible in the system; additionally, the discrete scattering loss from the LISA structures can be approximated as a continuous exponential loss in the system, which further emphasizes that the choice of the sampling rate, and the minimum coupling to backward modes at each LISA structure, which preserves the state fidelity as detailed in the next section. Similar technique of etching nanoholes in a topological photonic circuit consisting of ring resonators was recently realized [60].

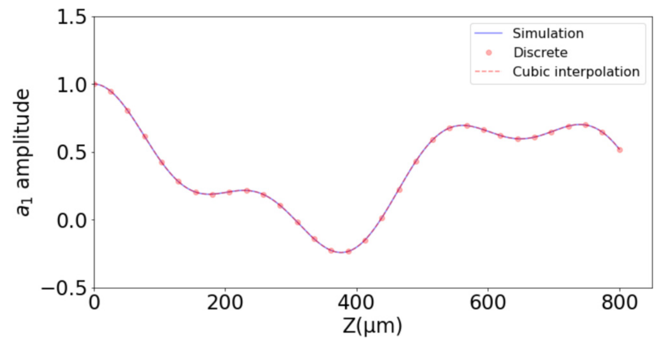

FIG. 13. Sampling and energy spectrum. Light dynamics in the edge lattice site measured continuously (solid blue line), sampled at 25 μm (red circles), and fitted from the discrete measurements using cubic spline interpolation (dashed red line).

APPENDIX F: STATE-VECTOR FIDELITY FOR SSH LATTICE WITH UNIFORM LOSS

The introduction of scattering sites in the SSH lattice plays an important role in probing the light dynamics in the nanosized waveguides of Si_3N_4, in addition to offering a single-shot method to measure the correlation function. The challenge with such an approach is the introduction of nonuniform loss in a single site of the lattice, which can alter the propagating-state fidelity. Our approach to combat such an effect is demonstrated in the SEM image shown in Fig. 12(a). In the reported SSH lattice, $t_1 = 0.0126\ \mu\text{m}^{-1}$ and $t_2 = 0.0063\ \mu\text{m}^{-1}$, corresponding to coupling lengths of 124 μm and 249 μm, respectively. Provided that uniform losses are introduced to the entire SSH lattice on length scales smaller than $1/t_1$ and $1/t_2$, the discrete losses from the scattering sites can be approximated as continuous Beer-Lambert relation affecting the whole lattice sites equally. In the fabricated device, we sample the edge waveguide, then

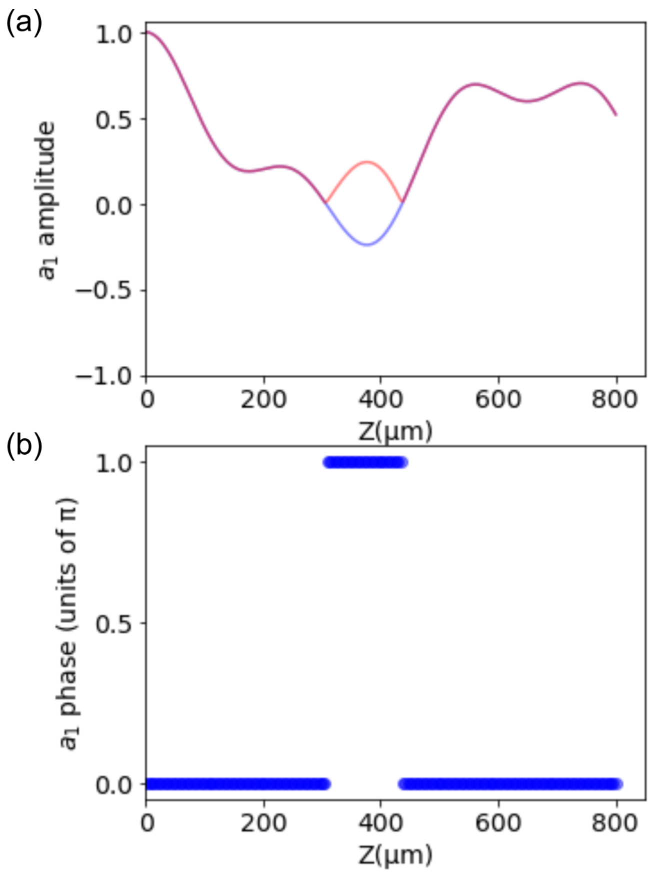

FIG. 14. Phase information of the edge lattice site. (a) Field amplitude in the edge lattice site. The blue curve contains the phase information while the red one takes the square root of the intensity. (b) Phase of the amplitude; a phase jump of π occurs when the light ray reflects off the lattice boundary.

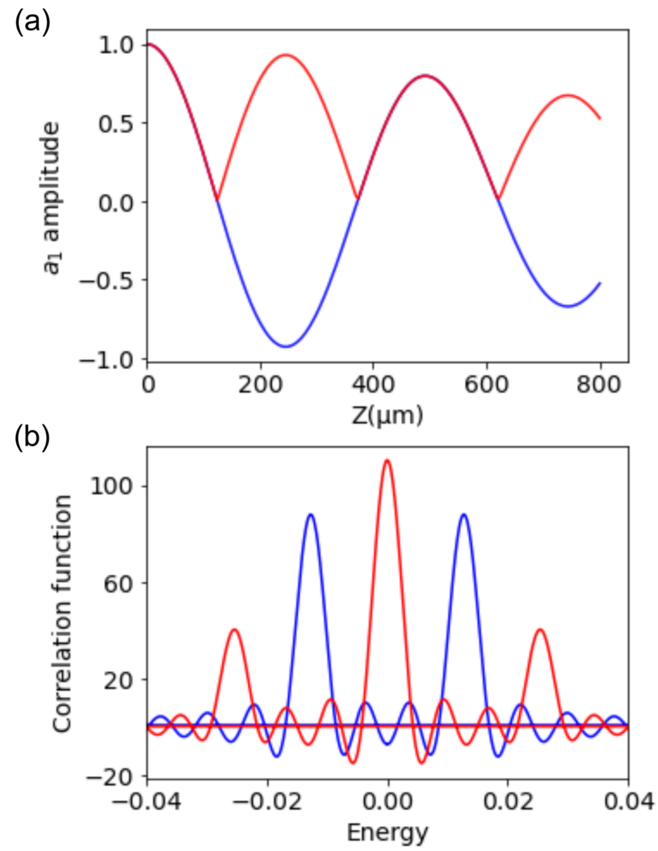

FIG. 15. Phase of the amplitude effect on the energy spectrum. (a) Field amplitude in the edge lattice site. The blue curve contains the phase information, while the red one takes the square root of the intensity. (b) Energy spectrum exhibits a zero-energy peak if the sign of the field is ignored (red curve), which should not be observed in the trivial lattice case considered.

introduce a uniform loss to the remaining 14 waveguides at 5 μm displacement along the propagation direction, much smaller than the coupling lengths in the system. The whole unit cell consisting of an edge-waveguide sampler and a uniform loss in the remainder of the lattice, is repeated at 25 μm period. To verify the minimum effect of the loss elements on the fidelity of the propagating states, we simulated the fabricated lattices using the algorithm depicted in Fig. 12(b). Light is injected through the edge waveguide and a unitary evolution operator is applied to the system to advance the state by 5 μm. After that, (1) loss is introduced to the input waveguide, then the state is renormalized, (2) a unitary evolution operator is applied to the system to advance the state by 5 μm, (3) loss is introduced to the remaining lattice sites, then state-renormalization, and, finally, (4) a unitary evolution operator is applied to the system to advance the state by 20 μm. The algorithm is repeated to span the total device length of 800 μm. The state fidelity is calculated through the inner product with an output state from an identical lossless lattice. Figure 12(c) shows a two-dimensional plot of the state fidelity at the output of the device for different disorder strength V/t_1 and loss asymmetry in the input waveguide compared to the remainder of the lattice $\mathrm{Loss}_{\mathrm{array}}/\mathrm{Loss}_{\mathrm{excitation}-WG}$. The result demonstrates that at such sampling period, with close to unity ratio between the two loss factors in the system, the state fidelity is close to unity.

To construct the energy spectrum from the autocorrelation function, there are two important parameters to consider [61]. The first is the resolution of the energy spectrum, which is directly related to the length of the sampling period. Our method provides an attractive approach for constructing a high-resolution energy spectrum through extending the length of the device, at the same time enabling a single shot method for achieving this. The second is the sampling rate relationship with the spectral range of the constructed signal, given by the Nyquist-Shannon sampling theorem [62]. Perfect reconstruction of the autocorrelation function is satisfied for energies $E < E_{\mathrm{sampling}}/2$. Considering the energy spectrum of the system [Fig. 1(a) in the main text], the chosen sampling period of 25 μm is carefully selected to enable long collection lengths of the light dynamics, and at the same time provide enough bandwidth to sample the first symmetric energy peaks of the system with respect to the zero-energy point.

Figure 13 shows the simulation results of a sampled field amplitude, 32 samples were taken in total using a 25 μm step, similar to the experiment setup. The dashed red curve

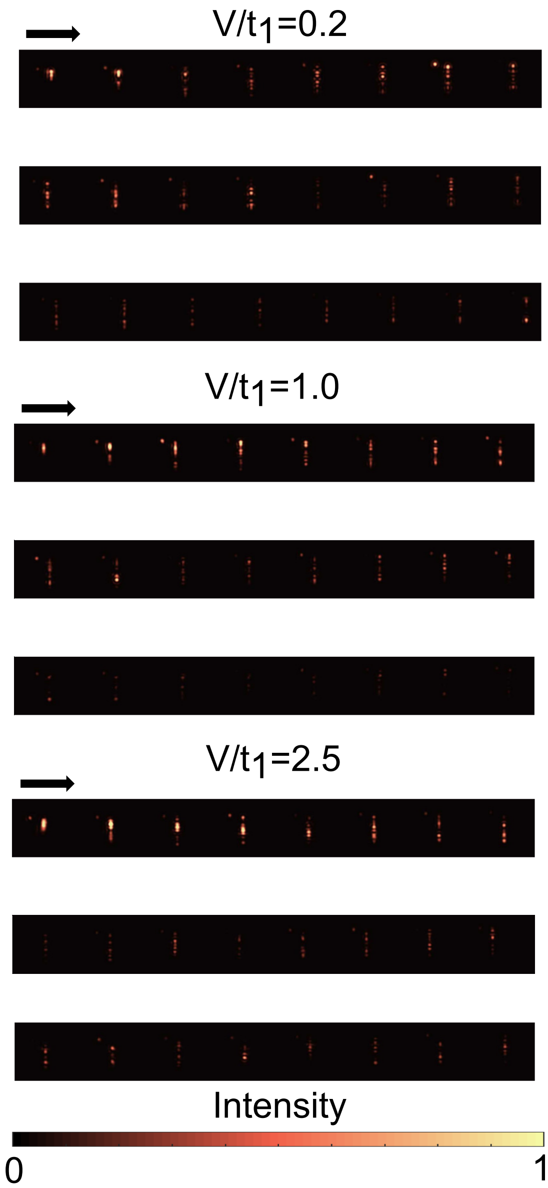

FIG. 16. Top intensity measurement of the scattered light from SSH lattices at three disorder values $V/t_1 = 0.2, 1$ and 2.5. The total sampled-length of the autocorrelation function is 700 μm, with 25 μm sampling period.

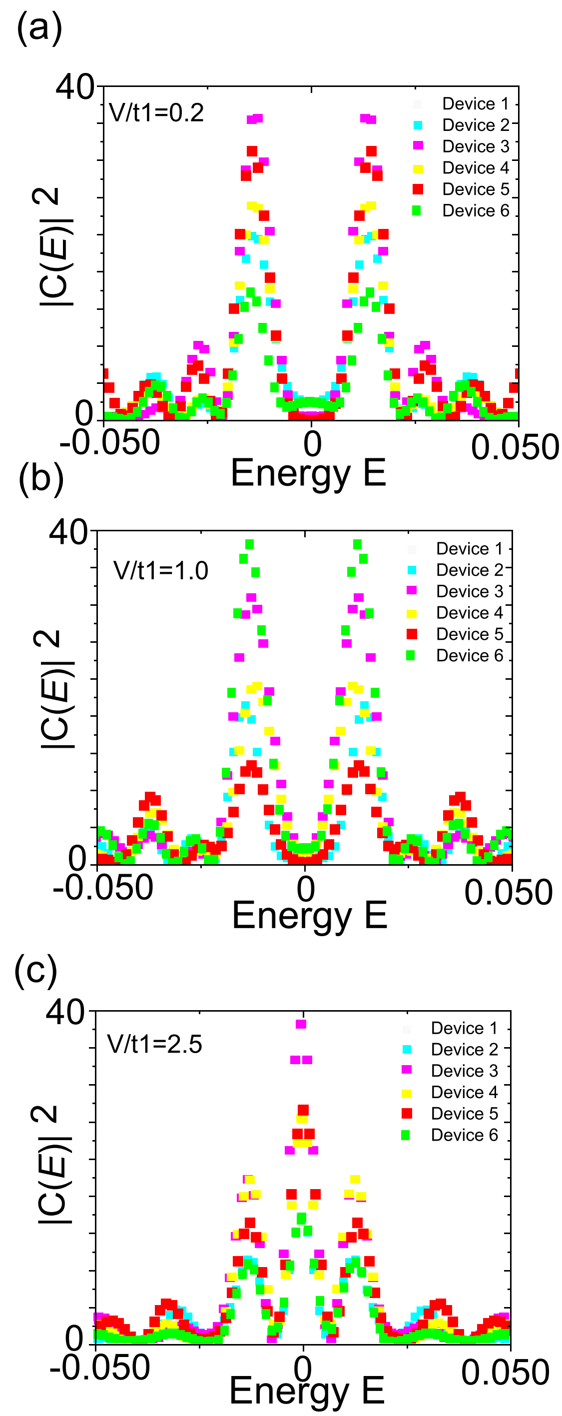

FIG. 17. Full data set of extracted energy spectrum. Eighteen devices were tested in total, six for each operating regime of the band diagram at (a) $V/t_1 = 0.2$, (b) $V/t_1 = 1$, and (c) $V/t_1 = 2.5$.

is given by the one-dimensional cubic spline interpolation of the discrete points. Comparing the recovered field distribution to the continuous field sampling limit shown in blue, we conclude that the discrete data points in the experiment provide a sufficient sampling rate to reproduce the continuous flow of light as discussed earlier.

APPENDIX G: PHASE INFORMATION OF THE EDGE STATE

To construct the energy spectrum of the propagating state, both the field amplitude and phase information are needed. The phase information is typically lost in an intensity-based imaging experiment. The issue we are dealing with here is to determine the sign of the amplitude. The π phase jump occurs when the light hits the boundary of the lattice (or full reflection). The amplitude will gradually decrease to 0 and then rise again. This zero point will indicate the flip point. In the ideal case, we could extract the discrete points showing the absolute values of the amplitude, then we can find that the flip occurs whenever there is a stationary point (also the local minimum). Figures 14(a) and 14(b) show the amplitude and phase of the edge lattice site; the binary phase simplifies the task of calculating the energy considerably, with no need of applying a sophisticated technique for phase retrieval.

It should be emphasized that the phase information in the amplitude is essential to determine the zero-peak energy. If we assume all the values to be positive (ignoring the phase jump at the boundary), then the FT results will also change accordingly, as exemplified in Figs. 15(a) and 15(b).

APPENDIX H: ADDITIONAL TOP-IMAGING DATA

In total, 28 intensity samples are measured for the edge state as it propagates in the fabricated SSH lattices. The autocorrelation function is collected for a total length of 700 μm (total length of the lattice is 800 μm), with 25 μm sampling period. In the main text (Fig. 3), only a subset of the data corresponding to a propagation distance of 200 μm is included; the full data set is presented here in Fig. 16. The images were collected with a CCD camera at an integration time of 1-2 ms, with a signal gain of 100.

APPENDIX I: ENERGY SPECTRUM DATA FOR ADDITIONAL DEVICES

Overall, 18 devices were examined, six for each operating regime of the band diagram, to probe the energy spectrum of the system at different disorder strengths: $V/t_1 = 0.2$, $V/t_1 = 1$, and $V/t_1 = 2.5$. The results are summarized in Fig. 17. We identify a consistent Anderson phase transition among devices manufactured on various fabrication runs as the disorder increases. The robustness of the topologically protected generalized winding number Q, which distinguishes between the trivial and nontrivial regimes, gives resistance against local disturbances caused by fabrication.

[1] L. Lu, J. D. Joannopoulos, and M. Soljacic, Topological photonics, Nat. Photonics **8**, 821 (2014).

[2] T. Ozawa, H. M. Price, A. Amo, N. Goldman, M. Hafezi, L. Lu, M. C. Rechtsman, D. Schuster, J. Simon, O. Zilberberg, and I. Carusotto, Topological photonics, Rev. Mod. Phys. **91**, 015006 (2019).

[3] D. Smirnova, D. Leykam, Y. Chong, and Y. Kivshar, Nonlinear topological photonics, Appl. Phys. Rev. **7**, 021306 (2020).

[4] D. T. H. Tan, Topological silicon photonics, Adv. Photonics Res. **2**, 2100010 (2021).

[5] F. D. M. Haldane and S. Raghu, Possible Realization of Directional Optical Waveguides in Photonic Crystals with Broken Time-Reversal Symmetry, Phys. Rev. Lett. **100**, 013904 (2008).

[6] Z. Wang, Y. Chong, J. D. Joannopoulos, and M. Soljačić, Observation of unidirectional backscattering-immune topological electromagnetic states, Nature (London) **461**, 772 (2009).

[7] M. C. Rechtsman, Y. Plotnik, J. M. Zeuner, D. Song, Z. Chen, A. Szameit, and M. Segev, Topological Creation and Destruction of Edge States in Photonic Graphene, Phys. Rev. Lett. **111**, 103901 (2013).

[8] M. Hafezi, S. Mittal, J. Fan, A. Migdall, and J. M. Taylor, Imaging topological edge states in silicon photonics, Nat. Photonics **7**, 1001 (2013).

[9] M. Hafezi, E. A. Demler, M. D. Lukin, and J. M. Taylor, Robust optical delay lines with topological protection, Nat. Phys. **7**, 907 (2011).

[10] M. C. Rechtsman, J. M. Zeuner, Y. Plotnik, Y. Lumer, D. Podolsky, F. Dreisow, S. Nolte, M. Segev, and A. Szameit, Photonic floquet topological insulators, Nature (London) **496**, 196 (2013).

[11] X. Cheng, C. Jouvaud, X. Ni, S. H. Mousavi, A. Z. Genack, and A. B. Khanikaev, Robust reconfigurable electromagnetic pathways within a photonic topological insulator, Nat. Mater. **15**, 542 (2016).

[12] G. Jotzu, M. Messer, R. Desbuquois, M. Lebrat, T. Uehlinger, D. Greif, and T. Esslinger, Experimental realization of the topological haldane model with ultracold fermions, Nature (London) **515**, 237 (2014).

[13] L. Lu, Z. Wang, D. Ye, L. Ran, L. Fu, J. D. Joannopoulos, and M. Soljačić, Experimental observation of weyl points, Science **349**, 622 (2015).

[14] X. Zhang, B.-Y. Xie, H.-F. Wang, X. Xu, Y. Tian, J.-H. Jiang, M.-H. Lu, and Y.-F. Chen, Dimensional hierarchy of higher-order topology in three-dimensional sonic crystals, Nat. Commun. **10**, 1 (2019).

[15] M. Atala, M. Aidelsburger, J. T. Barreiro, D. Abanin, T. Kitagawa, E. Demler, and I. Bloch, Direct measurement of the zak phase in topological bloch bands, Nat. Phys. **9**, 795 (2013).

[16] A. El Hassan, F. K. Kunst, A. Moritz, G. Andler, E. J. Bergholtz, and M. Bourennane, Corner states of light in photonic waveguides, Nat. Photonics **13**, 697 (2019).

[17] M. I. Shalaev, W. Walasik, A. Tsukernik, Y. Xu, and N. M. Litchinitser, Robust topologically protected transport in photonic crystals at telecommunication wavelengths, Nat. Nanotechnol. **14**, 31 (2019).

[18] X.-T. He, E.-T. Liang, J.-J. Yuan, H.-Y. Qiu, X.-D. Chen, F.-L. Zhao, and J.-W. Dong, A silicon-on-insulator slab for topological valley transport, Nat. Commun. **10**, 872 (2019).

[19] J. Ma, X. Xi, and X. Sun, Topological photonic integrated circuits based on valley kink states, Laser Photonics Rev. **13**, 1900087 (2019).

[20] Z.-K. Shao, H.-Z. Chen, S. Wang, X.-R. Mao, Z.-Q. Yang, S.-L. Wang, X.-X. Wang, X. Hu, and R.-M. Ma, A high-performance topological bulk laser based on band-inversion-induced reflection, Nat. Nanotechnol. **15**, 67 (2020).

[21] X. Gao, L. Yang, H. Lin, L. Zhang, J. Li, F. Bo, Z. Wang, and Ling Lu, Dirac-vortex topological cavities, Nat. Nanotechnol. **15**, 1012 (2020).

[22] S. Mittal, E. A. Goldschmidt, and M. Hafezi, A topological source of quantum light, Nature (London) **561**, 502 (2018).

[23] Y. Zeng, U. Chattopadhyay, B. Zhu, B. Qiang, J. Li, Y. Jin, L. Li, A. G. Davies, E. H. Linfield, B. Zhang, Y. Chong, and Q. J. Wang, Electrically pumped topological laser with valley edge modes, Nature (London) **578**, 246 (2020).

[24] M. A. Bandres, S. Wittek, G. Harari, M. Parto, J. Ren, M. Segev, D. N. Christodoulides, and M. Khajavikhan, Topological insulator laser: Experiments, Science **359**, eaar4005 (2018).

[25] R.-J. Ren, Y.-H. Lu, Z.-K. Jiang, J. Gao, W.-H. Zhou, Y. Wang, Z.-Q. Jiao, X.-W. Wang, A. S. Solntsev, and X.-M. Jin, Topologically protecting squeezed light on a photonic chip, Photon. Res. **10**, 456 (2022).

[26] A. Blanco-Redondo, B. Bell, D. Oren, B. J. Eggleton, and M. Segev, Topological protection of biphoton states, Science **362**, 568 (2018).

[27] J.-L. Tambasco, G. Corrielli, R. J. Chapman, A. Crespi, O. Zilberberg, R. Osellame, and A. Peruzzo, Quantum interference of topological states of light, Sci. Adv. **4**, eaat3187 (2018).

[28] S. Barik, A. Karasahin, C. Flower, T. Cai, H. Miyake, W. DeGottardi, M. Hafezi, and E. Waks, A topological quantum optics interface, Science **359**, 666 (2018).

[29] M. Wang, C. Doyle, B. Bell, M. J. Collins, E. Magi, B. J. Eggleton, M. Segev, and A. Blanco-Redondo, Topologically protected entangled photonic states, Nanophotonics **8**, 1327 (2019).

[30] Y. Wang, X.-L. Pang, Y.-H. Lu, J. Gao, Y.-J. Chang, L.-F. Qiao, Z.-Q. Jiao, H. Tang, and X.-M. Jin, Topological protection of two-photon quantum correlation on a photonic chip, Optica **6**, 955 (2019).

[31] J. Li, R.-L. Chu, J. K. Jain, and S.-Q. Shen, Topological Anderson Insulator, Phys. Rev. Lett. **102**, 136806 (2009).

[32] H. Jiang, L. Wang, Q.-f. Sun, and X. C. Xie, Numerical study of the topological anderson insulator in HgTe/CdTe quantum wells, Phys. Rev. B **80**, 165316 (2009).

[33] C. W. Groth, M. Wimmer, A. R. Akhmerov, J. Tworzydło, and C. W. J. Beenakker, Theory of the Topological Anderson Insulator, Phys. Rev. Lett. **103**, 196805 (2009).

[34] A. Altland, D. Bagrets, L. Fritz, A. Kamenev, and H. Schmiedt, Quantum Criticality of Quasi-One-Dimensional Topological Anderson Insulators, Phys. Rev. Lett. **112**, 206602 (2014).

[35] I. Mondragon-Shem, T. L. Hughes, J. Song, and E. Prodan, Topological Criticality in the Chiral-Symmetric AIII Class at Strong Disorder, Phys. Rev. Lett. **113**, 046802 (2014).

[36] P. Titum, N. H. Lindner, M. C. Rechtsman, and G. Refael, Disorder-Induced Floquet Topological Insulators, Phys. Rev. Lett. **114**, 056801 (2015).

[37] C. Liu, W. Gao, B. Yang, and S. Zhang, Disorder-Induced Topological State Transition in Photonic Metamaterials, Phys. Rev. Lett. **119**, 183901 (2017).

[38] S. Longhi, Topological anderson phase in quasi-periodic waveguide lattices, Opt. Lett. **45**, 4036 (2020).

[39] S. Stützer, Y. Plotnik, Y. Lumer, P. Titum, N. H. Lindner, M. Segev, M. C. Rechtsman, and A. Szameit, Photonic topological anderson insulators, Nature (London) **560**, 461 (2018).

[40] G.-G. Liu, Y. Yang, X. Ren, H. Xue, X. Lin, Y.-H. Hu, H.-x. Sun, B. Peng, P. Zhou, Y. Chong, and B. Zhang, Topological anderson insulator in disordered photonic crystals, Phys. Rev. Lett. **125**, 133603 (2020).

[41] E. J. Meier, F. A. An, A. Dauphin, M. Maffei, P. Massignan, T. L. Hughes, and B. Gadway, Observation of the topological anderson insulator in disordered atomic wires, Science **362**, 929 (2018).

[42] J. Song, H. Liu, H. Jiang, Q.-f. Sun, and X. C. Xie, Dependence of topological anderson insulator on the type of disorder, Phys. Rev. B **85**, 195125 (2012).

[43] A. Girschik, F. Libisch, and S. Rotter, Topological insulator in the presence of spatially correlated disorder, Phys. Rev. B **88**, 014201 (2013).

[44] Y. Kuno, Disorder-induced chern insulator in the harper-hofstadter-hatsugai model, Phys. Rev. B **100**, 054108 (2019).

[45] W. P. Su, J. R. Schrieffer, and A. J. Heeger, Solitons in Polyacetylene, Phys. Rev. Lett. **42**, 1698 (1979).

[46] J.-W. Wang, F. Sciarrino, A. Laing, and M. G. Thompson, Integrated photonic quantum technologies, Nat. Photonics **14**, 273 (2020).

[47] L. Chrostowski and M. Hochberg, *Silicon Photonics Design: From Devices to Systems* (Cambridge University Press, Cambridge, UK, 2015).

[48] S. Longhi, Metal-insulator phase transition in a non-hermitian aubry-andré-harper model, Phys. Rev. B **100**, 125157 (2019).

[49] D. Leykam and D. A. Smirnova, Probing bulk topological invariants using leaky photonic lattices, Nat. Phys. **17**, 632 (2021).

[50] G. Corrielli, G. Della Valle, A. Crespi, R. Osellame, and S. Longhi, Observation of Surface States with Algebraic Localization, Phys. Rev. Lett. **111**, 220403 (2013).

[51] M. Golshani, S. Weimann, Kh. Jafari, M. Khazaei Nezhad, A. Langari, A. R. Bahrampour, T. Eichelkraut, S. M. Mahdavi, and A. Szameit, Impact of Loss on the Wave Dynamics in Photonic Waveguide Lattices, Phys. Rev. Lett. **113**, 123903 (2014).

[52] A. Schumer, Y. G. N. Liu, J. Leshin, L. Ding, Y. Alahmadi, A. U. Hassan, H. Nasari, S. Rotter, D. N. Christodoulides, P. LiKamWa, and M. Khajavikhan, Topological modes in a laser cavity through exceptional state transfer, Science **375**, 884 (2022).

[53] I. C. Fulga, F. Hassler, A. R. Akhmerov, and C. W. J. Beenakker, Scattering formula for the topological quantum number of a disordered multimode wire, Phys. Rev. B **83**, 155429 (2011).

[54] M. Segev, Y. Silberberg, and D. N. Christodoulides, Anderson localization of light, Nat. Photonics **7**, 197 (2013).

[55] A. W. Elshaari, W. Pernice, K. Srinivasan, O. Benson, and V. Zwiller, Hybrid integrated quantum photonic circuits, Nat. Photonics **14**, 285 (2020).

[56] A. W. Elshaari, I. E. Zadeh, A. Fognini, M. E. Reimer, D. Dalacu, P. J. Poole, V. Zwiller, and K. D. Jöns, On-chip single photon filtering and multiplexing in hybrid quantum photonic circuits, Nat. Commun. **8**, 379 (2017).

[57] I. E. Zadeh, A. W. Elshaari, K. D. Jöns, A. Fognini, D. Dalacu, P. J. Poole, M. E. Reimer, and V. Zwiller, Deterministic integration of single photon sources in silicon based photonic circuits, Nano Lett. **16**, 2289 (2016).

[58] A. W. Elshaari, I. E. Zadeh, K. D. Jons, and V. Zwiller, Thermo-optic characterization of silicon nitride resonators for cryogenic photonic circuits, IEEE Photonics. **8**, 2701009 (2016).

[59] W. Huanga, Y. Chen, X. Qu, S. Yin, X. Shi, X. Xiongb, W. Zhangc, Z. Qin, and Y. Zhang, Complete and robust light transfer in three-waveguide coupler by shortcut to adiabaticity, AIP Adv. **10**, 095104 (2020).

[60] H. Zhao, X. Qiao, T. Wu, B. Midya, and S. Longhi, and L. Feng, Non-Hermitian topological light steering, Science **365**, 1163 (2019).

[61] S. V. Vaseghi, *Advanced Digital Signal Processing and Noise Reduction* (John Wiley and Sons, Hoboken, New Jersey, United States, 2008).

[62] C. L. Shannon, Communication in the presence of noise, Proc. IREE **37**, 232969 (1949).